

## ARTICLE OPEN



# Historical footprints and future projections of global dust burden from bias-corrected CMIP6 models

Jun Liu<sup>1</sup>, Xiaofan Wang<sup>1</sup>, Dongyou Wu<sup>1</sup>, Hailun Wei<sup>2</sup>, Yu Li<sup>3</sup> and Mingxia Ji<sup>1</sup>

Dust aerosols significantly affect the Earth's climate, not only as a source of radiation, but also as ice nuclei, cloud condensation nuclei and thus affect CO<sub>2</sub> exchange between the atmosphere and the ocean. However, there are large deviations in dust model simulations due to limited observations on a global scale. Based on ten initial Climate Models Intercomparison Project Phase Six (CMIP6) models, the multi-model ensemble (MME) approximately underestimates future changes in global dust mass loading (DML) by 7–21%, under four scenarios of shared socioeconomic pathways (SSPs). Therefore, this study primarily constrains the CMIP6 simulations under various emission scenarios by applying an equidistant cumulative distribution function (EDCDF) method combined with the Modern-Era Retrospective Analysis for Research and Applications version 2 (MERRA2) datasets based on observation assimilation. We find that the results (19.0–26.1 Tg) for 2000–2014 are closer to MERRA2 (20.0–24.8 Tg) than the initial simulations (4.4–37.5 Tg), with model deviation reduced by up to 75.6%. We emphasize that the DML during 2081–2100 is expected to increase significantly by 0.023 g m<sup>-2</sup> in North Africa and the Atlantic region, while decreasing by 0.006 g m<sup>-2</sup> in the Middle East and East Asia. In comparison with internal variability and scenario uncertainty, model uncertainty accounts for more than 70% of total uncertainty. When bias correction is applied, model uncertainty significantly decreases by 65% to 90%, resulting in a similar variance contribution to internal variability.

*npj Climate and Atmospheric Science* (2024)7:1; <https://doi.org/10.1038/s41612-023-00550-9>

## INTRODUCTION

Dust is one of the major light-absorbing components of atmospheric aerosol, originating in desert regions, agricultural and industrial activities<sup>1–5</sup>. As well as absorbing radiation, dust scatters heat and produces a net negative forcing. Moreover, it also provides iron and bio-essential trace elements to the marine phytoplankton<sup>6</sup>, thus affecting CO<sub>2</sub> exchange between the atmosphere and the ocean<sup>7</sup>. A large portion of dust emissions can be attributed to desert regions in North Africa, East Asia, Central Asia, Australia, and North America<sup>8,9</sup>. Statistically, the total dust emission contributes 1000–2150 Tg per year globally since 2001<sup>10,11</sup>, which is approximately half of the total tropospheric aerosols<sup>12–14</sup>. The westerly circulation can carry Asian dust to Japan, South Korea, and even across the Pacific to the United States and the Arctic<sup>15–20</sup>. Moreover, North American dust is also transported across the Atlantic to Europe via the westerly circulation<sup>21</sup>. North African dust can be transported to the Americas<sup>22</sup>. Consequently, numerous studies have examined the spatiotemporal variations, optical properties, and radiative forcing of dust aerosols using in-situ observations<sup>23–30</sup>, satellite remote sensing<sup>31–35</sup>, and model simulations<sup>36–38</sup>.

Model simulations provide information on spatio-temporal changes in global dust aerosol and enable predictions of future trends<sup>39–41</sup>. In recent years, the major properties of dust aerosols have been recognized systematically using results from CMIP5 and CMIP6 models<sup>42–45</sup>. However, Kok et al.<sup>46</sup> reported significant deviations in model simulations of the impact of dust aerosol on global energy budgets and regional climates. Pu & Ginoux<sup>40</sup> reported that the majority of CMIP5 models are incapable of simulating dust aerosol variability or capturing the relationship between dust aerosols and local controlling factors (e.g., wind

speed, bare ground, and precipitation). Wang et al.<sup>41</sup> showed that almost all CMIP6 models failed to capture the long-term trends of aerosol optical depth (AOD) over Asia from 2006 to 2014. Even though the CMIP models can reproduce the observed “dust belt”, there are still considerable differences in the spatial distributions of the dust belt as simulated by different models<sup>43,47</sup>. As a result, challenges remain in accurately predicting future trends in dust aerosols from historical in-situ observations and reanalysis datasets.

Model simulations of dust aerosol show large deviations as a result of uncertainties triggered by different socioeconomic pathways, model self-errors, and internal variability<sup>48,49</sup>. However, observational constraints can be used to correct model errors, thereby improving CMIP6 projections<sup>50</sup>. Observational constraints are mainly applied to climate prediction by comparing model results with those obtained from observational data, and examples of constraints include multi-model weighting<sup>45,51</sup>, the attribution constraint<sup>52,53</sup>, the emergence constraint<sup>54–56</sup>, and quantile mapping<sup>57–59</sup>. Currently, observational constraints have been applied to the prediction of global surface temperature, precipitation, extreme events, Arctic sea ice, and cloud feedbacks<sup>51,60–64</sup>. Such constraints have been used in the CMIP6 report for future projections of global surface temperature, ocean heat capacity, and sea level<sup>65</sup>. However, these robust constraints have not been applied to projections for other variables<sup>50,66</sup>. For example, Navarro-Racines et al.<sup>67</sup> found that the delta method can reduce the CMIP5 model bias by up to 50–70%. Using the variance adjustment technique, Hu & Zhou et al.<sup>68</sup> found that the uncertainty of summer precipitation in the Tibetan Plateau was reduced by 41.8% in comparison with raw data from CMIP5 models. The traditional quantile-based mapping method

<sup>1</sup>Key Laboratory for Semi-Arid Climate Change of the Ministry of Education, College of Atmospheric Sciences, Lanzhou University, Lanzhou, China. <sup>2</sup>Aviation Meteorological Center, Air Traffic Management Bureau, Civil Aviation Administration of China, Beijing, China. <sup>3</sup>College of Earth and Environmental Sciences, Lanzhou University, Lanzhou, China. ✉email: liyu@lzu.edu.cn; jimx@lzu.edu.cn

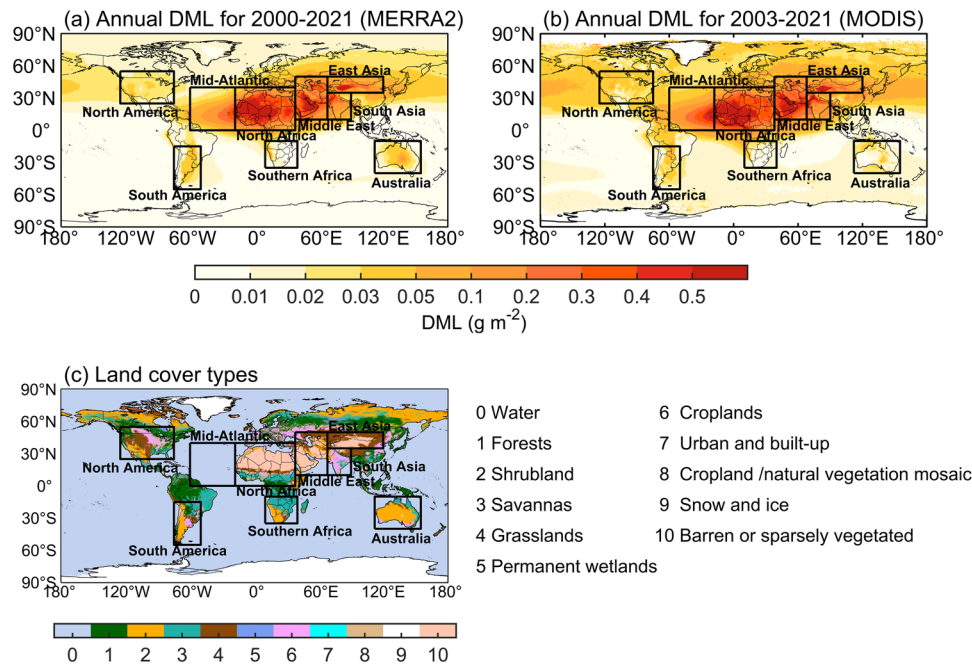


**Fig. 1** Spatial distribution of dust mass loading and land cover. The climatology of annual mean dust mass loading (DML;  $\text{g m}^{-2}$ ) based on (a) MERRA2 for 2000–2021 and (b) MODIS for 2003–2021. (c) Global land cover types retrieved by MODIS data. Black boxes indicate the boundaries of the nine selected study regions: (1) North Africa ( $18^{\circ}\text{W}$ – $38^{\circ}\text{E}$ ,  $0^{\circ}\text{N}$ – $40^{\circ}\text{N}$ ), (2) Mid-Atlantic ( $18^{\circ}\text{W}$ – $60^{\circ}\text{W}$ ,  $0^{\circ}\text{N}$ – $40^{\circ}\text{N}$ ), (3) Middle East ( $38^{\circ}\text{E}$ – $68^{\circ}\text{E}$ ,  $10^{\circ}\text{N}$ – $50^{\circ}\text{N}$ ), (4) East Asia ( $68^{\circ}\text{E}$ – $120^{\circ}\text{E}$ ,  $35^{\circ}\text{N}$ – $50^{\circ}\text{N}$ ), (5) South Asia ( $68^{\circ}\text{E}$ – $90^{\circ}\text{E}$ ,  $10^{\circ}\text{N}$ – $35^{\circ}\text{N}$ ), (6) Australia ( $112^{\circ}\text{E}$ – $155^{\circ}\text{E}$ ,  $10^{\circ}\text{S}$ – $40^{\circ}\text{S}$ ), (7) southern Africa ( $10^{\circ}\text{E}$ – $40^{\circ}\text{E}$ ,  $10^{\circ}\text{S}$ – $35^{\circ}\text{S}$ ), (8) South America ( $50^{\circ}\text{W}$ – $75^{\circ}\text{W}$ ,  $15^{\circ}\text{S}$ – $55^{\circ}\text{S}$ ), and (9) North America ( $75^{\circ}\text{W}$ – $125^{\circ}\text{W}$ ,  $25^{\circ}\text{N}$ – $55^{\circ}\text{N}$ ).

(cumulative distribution function; CDF) hypothesizes that the relationship between simulated and observed values during historical period is also valid for future period<sup>69,70</sup>. However, considering the difference between the CDFs for the future and reference periods, the EDCDF method applies a quantile-based mapping difference of the CDFs in the historical to match the climatic fields in the future period<sup>71</sup>. This method can be used to correct the mean and distribution range of a target variable, as well as to reduce model bias<sup>57,58</sup>.

Our previous study found an obvious reduction in future spring dust emissions in northern China from CMIP5 model outputs, with maximum reductions of  $4 \text{ g m}^{-2}$  in the Taklimakan Desert and  $8 \text{ g m}^{-2}$  in the Gobi Desert<sup>72</sup>. This is linked to decreased zonal winds and weakened temperature gradients caused by winter Arctic warming<sup>28,72</sup>. However, the uncertainties in model simulations of dust aerosol have not been addressed systematically. As a result, nine representative study areas were selected around the globe (North Africa, Mid-Atlantic, Middle East, East Asia, South Asia, Australia, southern Africa, South America, and North America), which are mainly grassland, barren or sparse vegetation and other surface types that are prone to dust emission (Fig. 1). A spatial climate and dust trend in Modern-Era Retrospective Analysis for Research and Applications version 2 (MERRA2) are largely similar to those in Moderate-resolution Imaging Spectroradiometer (MODIS). This is because MERRA2 assimilated bias-corrected AOD from Collection 5 MODIS after 2000, the Advanced Very High Resolution Radiometer (AVHRR) for 1980–2002 over ocean-only and other observation products<sup>73,74</sup>. Hence, we used MERRA2 reanalysis data in combination with the EDCDF method to constrain historical simulations of monthly dust mass loading (DML) in CMIP6 models for 2000–2014 and future projections for 2015–2100. The CMIP6 models are calibrated for the training period (15 years: 2000–2014), and the validation period is from 2015 to 2021. Simultaneously, the Taylor diagram<sup>75</sup> and uncertainty sources partitioning<sup>76,77</sup> methods are applied to evaluate uncertainty in DML projections before and after bias correction. We focus on future spatiotemporal variations in DML in typical

regions under shared socioeconomic pathway (SSP) scenarios (SSP126, SSP245, SSP370, and SSP585). This study seeks to illustrate future changes in global DML and its uncertainty sources, which is important for improving dust parameters in climate models and accurately assessing the radiation effects of global dust aerosols.

## RESULTS

### Global DML simulation

Figure 2 shows the annual mean climatology of DML for MERRA2, the CMIP6 multi-model ensemble (MME), and each individual model (see Supplementary Table 1) for 2000–2014. We found that CMIP6 models generally capture the major “dust belt” feature that extends from North Africa, Middle East, and Central Asia to East Asia, which is consistent with previous studies<sup>47,78</sup>. According to Fig. 2a, MERRA2 reanalysis is in good agreement with MME simulations (Fig. 2b), with a Taylor skill score (SS) approaching 1. However, the SS values for half of the models remain below 0.8 (Fig. 2 (1), (6), (7), (8), and (9)), suggesting that the spatial pattern and magnitude of global DML are not adequately simulated. Compared with MERRA2, the DML simulated by models CESM2-WACCM, MIROC-ES2L, and NorESM2-MM is significantly lower in the west and higher in the east of North Africa. Moreover, the total global DML simulated by CMIP6 during the period 2000–2014 ranges from 5 to 32 Tg, which is smaller than the range in CMIP5 (3 to 42 Tg) noted by Wu et al.<sup>43</sup>. We also observed significant differences in dust source regions between MERRA2 and the models, such as MIROC6 and NorESM2-MM, which simulate significantly less dust in the atmosphere (5.3 and 9.3 Tg, respectively), with SS values of 0.23 and 0.50, respectively.

The simulation of interannual variation and magnitude of DML varies significantly between models (Supplementary Fig. 1). For example, the DML simulated by the MIROC6 and NorESM2-MM models is significantly smaller compared with the reanalysis dataset over North Africa, the Mid-Atlantic, Middle East, and South

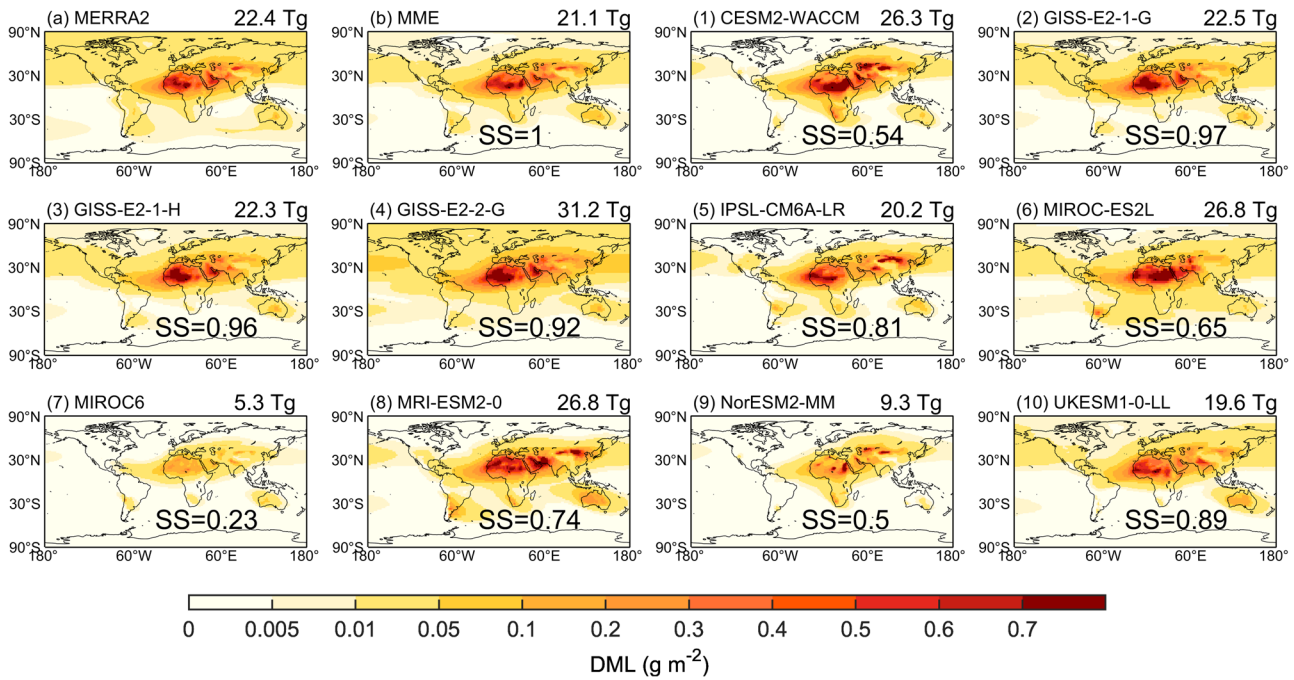


**Fig. 2 Spatial distribution of annual mean dust mass loading.** The climatology of dust mass loading (DML;  $\text{g m}^{-2}$ ) for 2000–2014 based on (a) MERRA2 and (b) the CMIP6 multi-model ensemble (MME). (1)–(10) Results of individual CMIP6 models. The number at top right in each panel denotes the global total dust burden (Tg), and the number within each panel is the Taylor skill score (SS) of the individual model.

Asia. Moreover, the MME simulations of DML seasonal cycles are basically in agreement with the reanalysis dataset (Supplementary Fig. 2). There are noticeable discrepancies among models in North Africa, East Asia, Australia, southern Africa, and South America, as well as large discrepancies in dust optical depth (DOD) and dust emission<sup>44,47</sup>. Even though the CMIP6 MME is capable of accurately simulating the annual variation in DML and seasonal cycles, the simulation deviation of individual models remains high, indicating the importance of bias correction in predicting future changes in DML across the globe.

#### Performance assessment of bias-corrected CMIP6 models

The EDCDF method was then applied to correct the DML from CMIP6 models. Figure 3 compares the mean total dust loading of the MODIS and CMIP6 models from January to December for 2003–2014 over the globe, as well as nine study regions before and after EDCDF bias correction. Before the correction (insets), CMIP6 MMEs have a good correlation with the observation on average ( $R > 0.5$ ,  $P < 0.01$ ) in other regions, except for southern Africa (Fig. 3h). As compared with observation results, the total dust loadings from individual models vary widely, with deviations of up to 10 times in the Mid-Atlantic, Australia, southern Africa, and South America. After the bias correction, simulations of total dust loading are greatly improved, and the correlation coefficient between MMEs and observation is 0.94 ( $P < 0.01$ ) in the globe (Fig. 3a), up from  $-0.16$  ( $p > 0.05$ ) before correction to 0.6 ( $p < 0.01$ ) in southern Africa (Fig. 3h). In addition, the uncertainty ranges of individual models are significantly reduced by more than 50% compared with the observation. As shown in Supplementary Fig. 3, the probability density function (PDF) distribution of the monthly DML bias reveals that the simulation deviation of dust in typical areas of the world decreased significantly before and after the correction. Although the corrected MME does not improve significantly, each individual model shows distinct improvements in global dust simulation (Fig. 3k). The corrected total dust burden is also much closer to the results of MERRA2 reanalysis (20.0–24.8 Tg), with a simulated

range of 19.0–26.1 Tg, and the model bias is reduced by up to 75.6% compared with uncorrected models (4.4–37.5 Tg). Moreover, according to the MERRA2 reanalysis (Supplementary Fig. 4), the global mean dust burden during 2015–2021 is 17.7 Tg, of which 8.3 Tg is found in North Africa, 3.2 Tg in the Middle East, 1.1 Tg in East Asia and 0.8 Tg in South Asia, respectively. The relative contributions of the major dust source regions to atmospheric loading are consistent with those reported by Kok et al.<sup>79</sup>. There is a significant decrease in the simulation deviation for these models (ESM2-WACCM, MIROC-ES2L, MIROC6, MRI-ESM2-0, and NorESM2-MM). Consequently, the bias-corrected method significantly improves the CMIP6 simulations of global DML.

To accurately reflect the simulation performance of trend in DML, we presented time series of DML from 1980 to 2100 based on MODIS, MERRA2, and CMIP6 models (Fig. 4). The MODIS and MERRA2 have a certain deviation in time variability, especially in the Middle East, South Asia, and North America. Additionally, there is an obvious jump in MERRA2 data before and after 2000, possibly due to MERRA2 assimilation of MODIS satellite and other observation products<sup>73,74</sup>. For this reason, MERRA2 products from 2000 to 2014 were used for model calibration. In comparison with the uncorrected results, the corrected CMIP6 models and MERRA2 show good consistency. Compared to the past, the bias-corrected global DML climatology is larger in South America, North America, and Middle East, and is smaller in North Africa, East Asia, Australia, and southern Africa. The Mid-Atlantic and South Asia have remained unchanged. In general, MERRA2 and MODIS DML trends are similar, except for East Asian trends which have increased and decreased, but the CMIP6 MME is able to accurately simulate these trends (Supplementary Fig. 5). However, previous studies based on ground stations and satellite observations have shown that dust occurrences in East Asia mainly shows a decrease from 2000s<sup>28</sup>, so the obvious increase from MERRA2 needs further study. In model simulations, spatial distributions of DML trends did not differ significantly before and after calibration (Supplementary Figs. 5–7). Even though the CMIP6 models do not simulate observed trends as well, they agree with observations over the Asian continent, the Mid-Atlantic, southern North Africa, and Middle

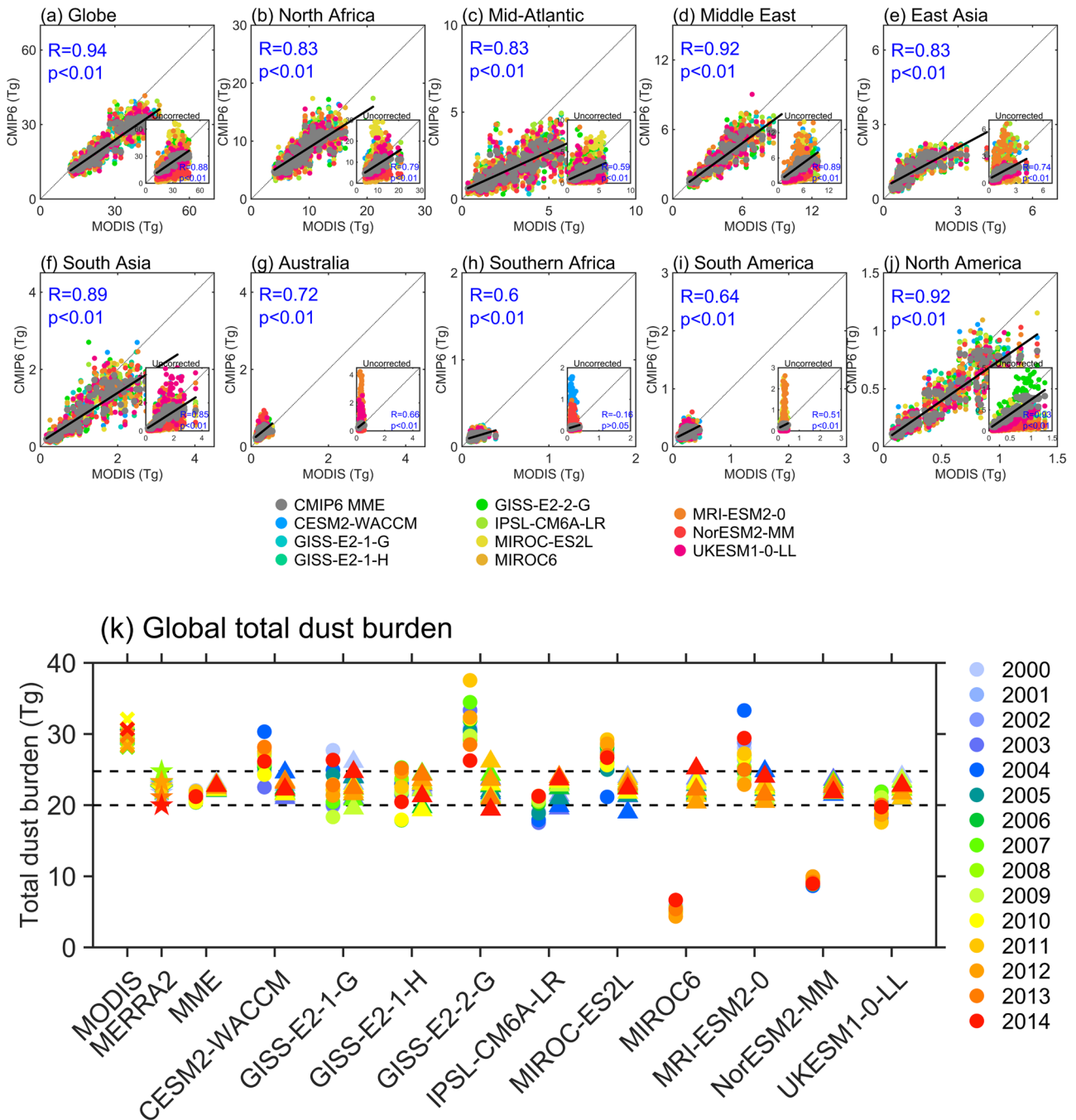


**Fig. 3 Comparison of total dust loading between CMIP6 models and MODIS products.** Scatterplots of mean total dust loading from January 2003 to December 2014 over the globe (**a**) and nine study regions (**b–j**) between MODIS and bias-corrected CMIP6 models. The colored dots represent different models, and the gray dots represent CMIP6 MME. The solid slope lines are the linear fitting between MODIS and CMIP6 MME, and the correlation coefficients ( $R$ ) and  $P$  values are shown in the blank space. The 1:1 dotted lines are plotted for reference. Here insets are uncorrected results. **k** Global annual total dust burden based on MODIS (cross) for 2003–2014 and MERRA2 (star), uncorrected (circle) and bias-corrected (triangle) CMIP6 models for 2000–2014. The upper and lower dotted lines are the maximum and minimum values of the MERRA2 reanalysis.

East. In contrast, the increase in the Mid-Atlantic is contrary to the results from 1982 to 2008 reported by Ridley et al.<sup>80</sup>. The EDCDF method mainly calibrates the magnitude deviation of model simulation, and does not significantly calibrate the trend<sup>57,58</sup>. However, except for the UKESM1-0-LL model, the spatial trends of future DML simulated by other CMIP6 models are consistent (Supplementary Figs. 8 and 9). Compared with all initial models, the bias-corrected models can more accurately depict the future dust changes.

### Future projection of global DML

In the future projections, we present the relative changes in global bias-corrected DML over the near-term (2021–2040), medium-term (2051–2070), and long-term (2081–2100) relative to the reference period (2000–2014) under the SSP126, SSP245, SSP370, and SSP585 scenarios (Fig. 5). The trend of DML after bias correction is relatively consistent with uncorrected results (Supplementary Fig. 10), but there is a certain deviation in magnitude (Supplementary Fig. 11). The corrected DML is lower

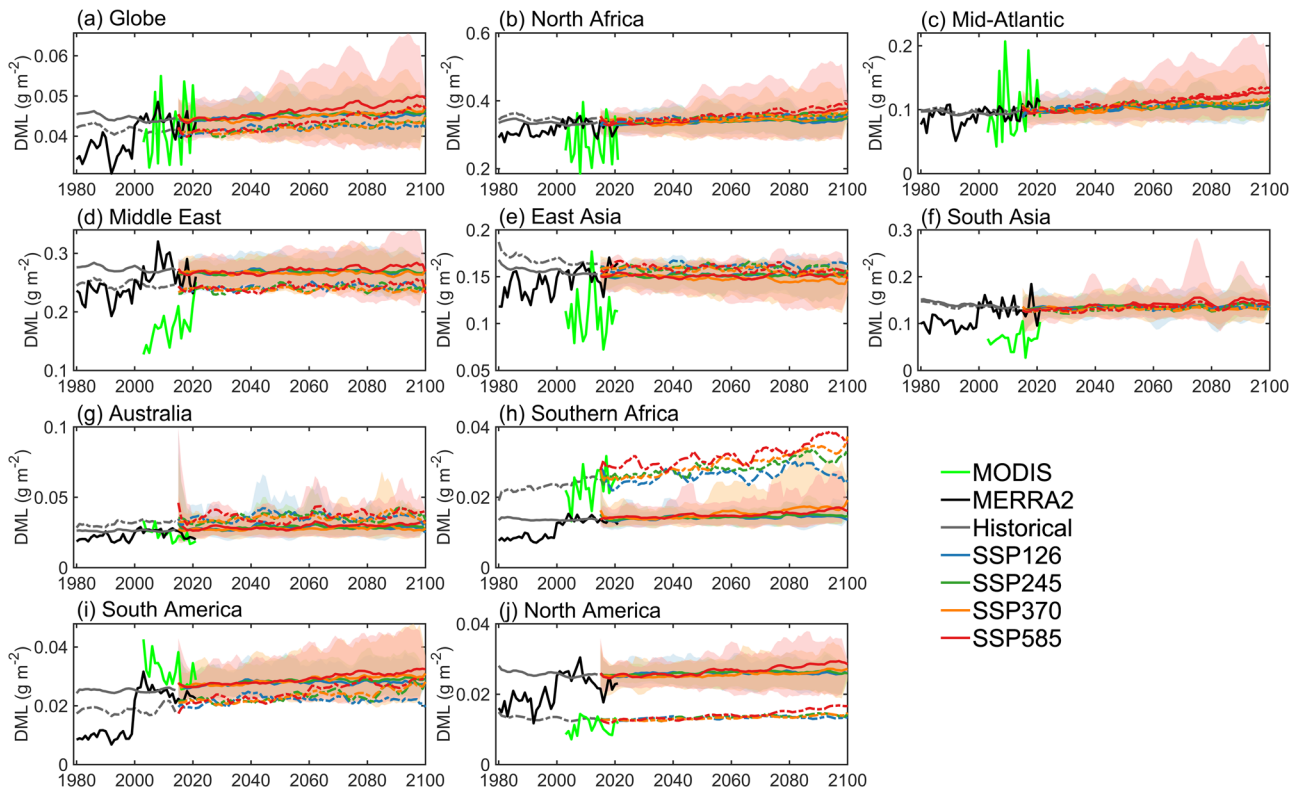


**Fig. 4** The temporal evolution in DML. DML ( $\text{g m}^{-2}$ ) over the globe (a) and nine study regions (b–j) are from uncorrected (dotted line) and bias-corrected (solid line) CMIP6 MME for 1980–2100, MODIS for 2003–2021, and MREEA2 for 1980–2021. Shading is the upper and lower boundaries in the 10 bias-corrected CMIP6 model outputs. The solid black lines are MERRA2 reanalysis results, and the green lines are MODIS results.

(up to  $-0.49 \text{ g m}^{-2}$ ) in eastern North Africa, southern Africa, East Asia and Australia. It is higher (up to  $0.22 \text{ g m}^{-2}$ ) in western North Africa and the middle-high latitudes of the Northern Hemisphere. The future changes in DML exhibit similar spatial patterns under the four SSP scenarios (Fig. 5). Relative to the historical period (2000–2014), the regional DML will continue to increase in the Mid-Atlantic, south of North America, South America, southern Africa, and Australia, while decreasing in the east of North Africa, Middle East, South Asia and East Asia from 2021 to 2100 under the SSP126, SSP245, SSP370 scenarios. In general, the DML is reduced by up to  $0.06$  ( $0.03$ )  $\text{g m}^{-2}$  in the Middle East and East Asia, while it increases by up to  $0.10$  ( $0.12$ )  $\text{g m}^{-2}$  in North Africa under the SSP370 (SSP585) scenario. Before 2040, the DML in North Africa increases in the west and decreases in the east. Then, it decreases slowly in the east and shifts to an increasing trend in the long term. Here a decrease in soil moisture (Supplementary Fig. 15) and an increase in surface wind speed (Supplementary Fig. 16) in the Sahara Desert are also conducive to dust emission (Supplementary Fig. 12). In the Middle East, dust is decreasing under the SSP370 due to enhanced dust wet deposition (Supplementary Fig. 13), dust emission suppression (Supplementary Fig. 12) due to increased soil moisture (Supplementary Fig. 15) and reduced surface wind speed (Supplementary Fig. 16), as well as possible irrigation expansion<sup>81</sup>. Under the SSP585, the near-term variation is similar to that in other scenarios, but in the medium and long-term, DML only decreases in East Asia, and increases significantly in the North Africa-Atlantic region, Middle East, northern South Asia, and southern Africa, up to  $0.12 \text{ g m}^{-2}$ . In East Asia, a decrease in DML during 2020–2100 is likely to be closely related to a decrease in dust storm frequency<sup>82</sup> and surface wind<sup>72</sup> (Supplementary Fig. 16), as well as an enhancement in precipitation (Supplementary Fig. 14) and dust wet deposition (Supplementary Fig. 13).

We also examined the changes in DML over the globe, as well as the nine selected regions during the long term (2081–2100) relative to the reference period (2000–2014; Fig. 6 and Supplementary Table 2). The global DML from the CMIP6 MME increases significantly under all scenarios, with the corrected DML increasing by up to  $0.003 \text{ g m}^{-2}$  under SSP585 scenario. Compared with the bias-corrected results, the initial MME underestimates the increase of global DML by 7% to 21% during the long term. Similarly, in North Africa and Mid-Atlantic region, DML increases under all scenarios, and this is underestimated slightly by the uncorrected CMIP6 models. Under the SSP585 scenario, the corrected DML increase over North Africa is up to  $0.023 \text{ g m}^{-2}$ , much higher than the  $0.016 \text{ g m}^{-2}$  under the SSP370 scenario. There is a decrease in the DMLs over the Middle East and East Asia, especially in East Asia under SSP370, with a reduction of  $0.006 \text{ g m}^{-2}$ , which is slightly less than before the correction ( $0.012 \text{ g m}^{-2}$ ). A recent study revealed that DML increases uniformly across North Africa and the downwind Atlantic as a result of increased dust emissions during the spring and summer months<sup>83</sup>. However, it decreases over East Asia due to enhanced local precipitation that promotes wet deposition<sup>45</sup> and decreased surface wind speed<sup>72,82</sup>, which is consistent with the results in this study. In South Asia, the DML varies greatly under different scenarios. SSP126 and SSP245 show no obvious change, but SSP370 shows a slight decrease and SSP585 shows a significant increase. Moreover, DMLs in Australia, southern Africa, South America, and North America also show an increase in all future scenarios.

#### Uncertainty assessment

We explored the fractional uncertainty of different uncertainty sources (internal variability, model uncertainty, and scenario

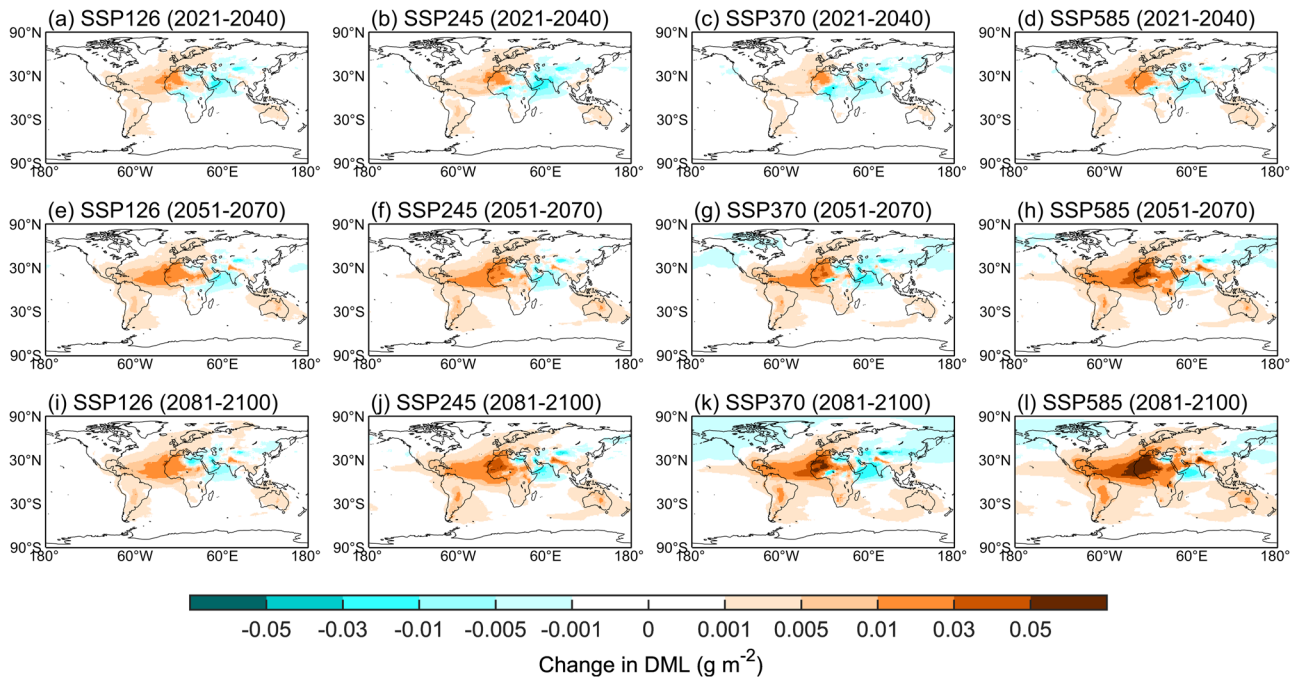


**Fig. 5 Future change of bias-corrected DML during different periods.** Spatial changes in the global bias-corrected DML ( $\text{g m}^{-2}$ ) relative to the historical period (2000–2014) for the (a–d) near-term (2021–2040), (e–h) medium-term (2051–2070), and (i–l) long-term (2081–2100) under the four SSP scenarios from the CMIP6 MME.

uncertainty) in DML of CMIP6 models before and after bias correction (Fig. 7). The fractional uncertainty is the prediction uncertainty divided by the expected mean change in global DML. Compared with uncorrected DML, the total uncertainty on a global scale decreased by 63–88% after bias correction. The model uncertainty is the most obvious reduction (75–92%), followed by the internal variability (19–65%), while the scenario uncertainty has no significant change. There are similar changes in uncertainties in typical regions as there are throughout the world. As a result of a large decline in model uncertainty of 92%, East Asia shows the largest decrease in total uncertainty (87.8%). However, the Mid-Atlantic region has the smallest declines in both total and model uncertainty, at 63.4% and 75%, respectively. While model, internal variability and scenario uncertainties decrease significantly in southern Africa and South America, reaching 89% (88.1%), 55.2% (64.2%), and 58.1% (56.2%), respectively.

For different lead times in the 21st century, the fraction of total variance due to individual uncertainties is also presented in Supplementary Figs. 17 and 18, respectively. Before bias correction, the main attribution of uncertainty is model uncertainty, with variance contributing more than 70%, followed by internal variability, and scenario uncertainty contributing less than 5%. After bias correction, the model uncertainty and internal variability are dominant at all lead times, but the proportions increase and decline with the increase of lead times respectively. Notably, the percentage contributed by scenario uncertainty is very small before and after bias correction. Supplementary Figure 19 and Fig. 8 show the proportion of three uncertainty sources in different lead times before and after bias correction respectively. With the exception of Europe and Australia, model uncertainty accounts for more than 80% of total uncertainty in most regions of the world at all lead times based on uncorrected models (Supplementary Fig. 19). After bias correction (Fig. 8), it is found that the contribution of model uncertainty and internal variability to the total uncertainty is dominated by the significant reduction of model uncertainty. Specifically, internal variability is an important source of uncertainty in the near-term (2021–2040), with most regions contributing more than 60%, and its proportion decreases

gradually with lead times. Unlike internal variability, contribution of model uncertainty in most parts of the world is below 40% in the near term (2021–2040) and increases to more than 50% in long term (2081–2100). The proportions of model uncertainty in Europe, northern Indian Ocean and Central Pacific region are below 50% at all lead times, and even as low as 1% in near term (2021–2040). It is clear that scenario uncertainty is rarely an important factor in triggering uncertainty. However, in the region between North and South America at the end of the century, scenario uncertainty is an important source of uncertainty, contributing up to 40%. Therefore, bias correction can effectively reduce the uncertainty of future predictions regarding dust aerosols, specifically model uncertainty.

## DISCUSSION

We used the MERRA2 and 10 CMIP6 models to explore the performance of global DML simulations. Approximately half of the models were unable to reproduce the spatial pattern of DML compared with MODIS observation and MERRA2 reanalysis for 2000–2014. In addition, the simulation of annual variations and seasonal cycles of DML varies greatly among models. Therefore, we applied the EDCDF method to correct 10 CMIP6 models and presented global climate change projections for the twenty-first century under the SSP126, SSP245, SSP370, and SSP585 scenarios. Results show that the EDCDF method can effectively lower the simulation deviation of DML from CMIP6 models, and does not significantly change the trend. The uncertainty ranges of individual models are significantly reduced by more than 50% compared with the reanalysis data on a monthly scale after bias correction. Compared with the uncorrected global total dust burden (4.4–37.5 Tg), the corrected models give values (19.0–26.1 Tg) closer to MERRA2 (20.0–24.8 Tg), and the model deviation is reduced by up to 75.6%. We further found that the initial CMIP6 MME underestimates the increase of global DML by 7% to 21% under all SSP scenarios. The spatial changes of DML before and after bias correction are basically consistent. Compared with the historical period (2000–2014), the DML will continue to increase

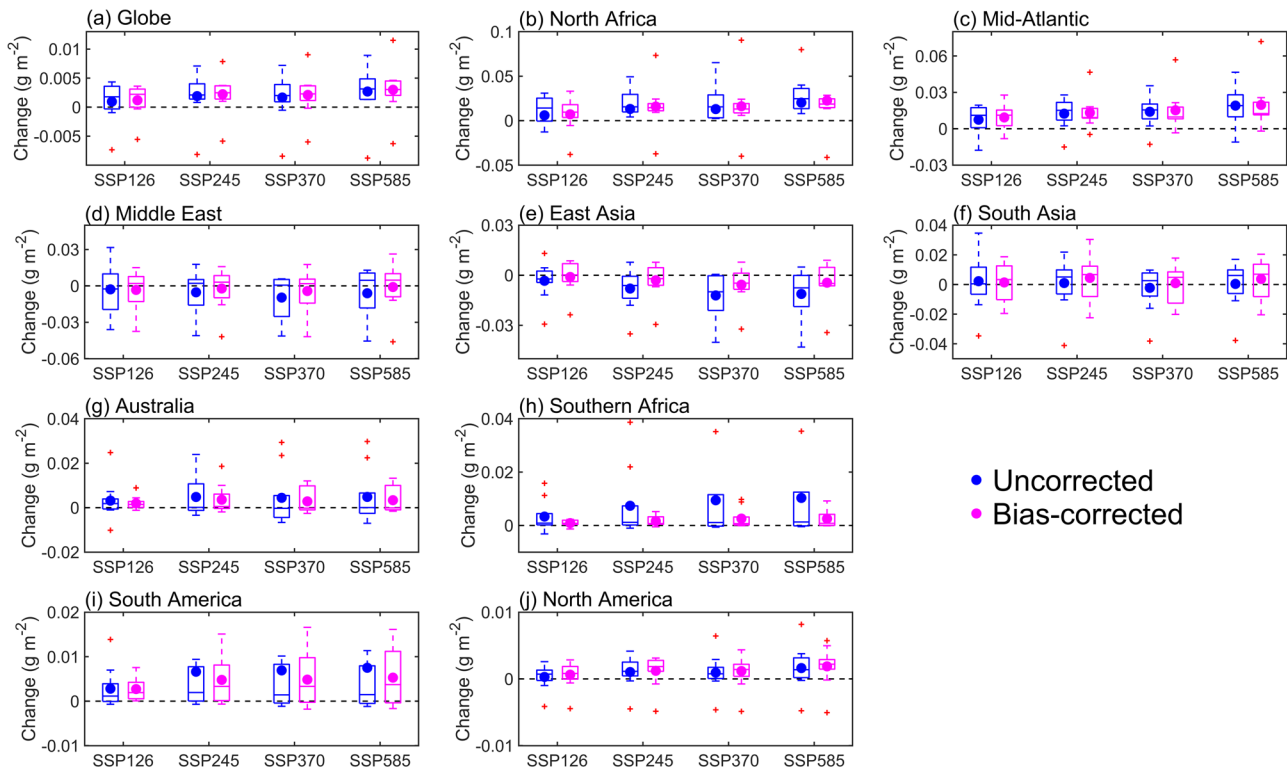


**Fig. 6** Future change of bias-corrected DML on four SSP scenarios. Distribution of changes in uncorrected (blue) and bias-corrected (purple) DML ( $\text{g m}^{-2}$ ) for the period 2081–2100 under the four SSP scenarios relative to the historical period (2000–2014) from the CMIP6 MME over the globe (a) and nine study regions (b–j). The box plots show the 25th and 75th percentiles as solid lines that define the box, the median value as the solid line within each box, the dots represent the changes from MME, the whiskers extend to the minimum and maximum, and the red crosses are outliers.

up to  $0.023 \text{ g m}^{-2}$  in the North Africa-Atlantic region, while it will decrease up to  $0.006 \text{ g m}^{-2}$  in the Middle East and East Asia during 2081–2100.

The analysis of uncertainty sources shows that model uncertainty is the main source of uncertainty in the simulation of future global DML, accounting for more than 70% of the total uncertainty, followed by internal variability and scenario uncertainty. Compared with uncorrected models, the application of the EDCDF method can significantly reduce the total uncertainty by 63–88%, and the reduction of the model uncertainty is as high as 75–92%. The bias correction method obviously changes the spatial patterns of global uncertainty sources. Before bias correction, there appears to be a similar distribution of uncertainties across the entire future period, namely that model uncertainty contributes the most, followed by internal variability, and scenario uncertainty contributes the least. After bias correction, model uncertainty and internal variability are the main sources of uncertainty, in which the internal variability contributes more than 60% in near term (2021–2040) and decreases with lead times. On the contrary, the proportion of model uncertainty is relatively small in near term, and up to more than 50% by 2100.

Based on MODIS and MERRA2, DML in North Africa has decreased, while models before and after the correction show an increase in western North Africa and a decrease in eastern North Africa (Supplementary Fig. 5). The previous study found that dust deviation in North African in models is due to errors in the surface wind field, rather than due to the dust emission processes<sup>84</sup>. Interestingly, both observations and models indicate an increasing trend of dust in the Mid-Atlantic in the historical (2000–2021) and future periods (2015–2100). Unlike Evan et al.<sup>85</sup> who concluded that the AVHRR data over the period 1982–2009 showed significant downward trends in dust optical depth over North Atlantic, as well as the CMIP5 data in the future,

resulting from the reduction of dust emissions and transport from Africa. Similarly, Ridley et al.<sup>80</sup> also indicated a reduction ( $\sim 10\%$  per decade) in dust optical depth over the Mid-Atlantic from 1982 to 2008 observed by the AVHRR satellite, due to a reduction in surface winds over dust source regions in Africa. We find that dust over the Mid-Atlantic has a rapid downward trend from the mid-1980s to 1995, then a steady fluctuation in the 2000s (Fig. 4c). This result, derived from MERRA2 assimilating AVHRR only-ocean data for 1980–2002, is consistent with the result of Evan et al.<sup>85</sup> from AVHRR satellite. For 2010–2021, MODIS and MERRA2 show an increasing trend for dust over the Mid-Atlantic (Fig. 4c), which is predicted to continue in the future by CMIP6. As mentioned above, the North African region has been experiencing increased dust emissions and higher surface wind speeds. However, the influencing factors (such as AMO<sup>86</sup>, NAO<sup>87</sup>, ENSO<sup>88</sup>, etc.) that produce this transition need further investigation in the future.

## METHODS

### MERRA2 reanalysis

MERRA2 is the latest version of the satellite-era global atmospheric reanalysis produced by the National Aeronautics and Space Administration (NASA) Global Modeling and Assimilation Office (GMAO) using the Goddard Earth Observing System Model (GEOS) version 5.12.4<sup>89</sup>. The GEOS model is coupled with the Goddard Chemistry Aerosol Radiation and Transport model (GOCART) aerosol module<sup>74</sup> to simulate five types of aerosols (dust, black carbon, organic carbon, sulfate, and sea salt) from 1980. MERRA2 includes assimilation of bias-corrected AOD derived from AVHRR and MODIS radiances. We acquired a time-averaged two-dimensional monthly mean data collection (avgM\_2d\_aer\_Nx), which included assimilated aerosol diagnostics (such as dust column

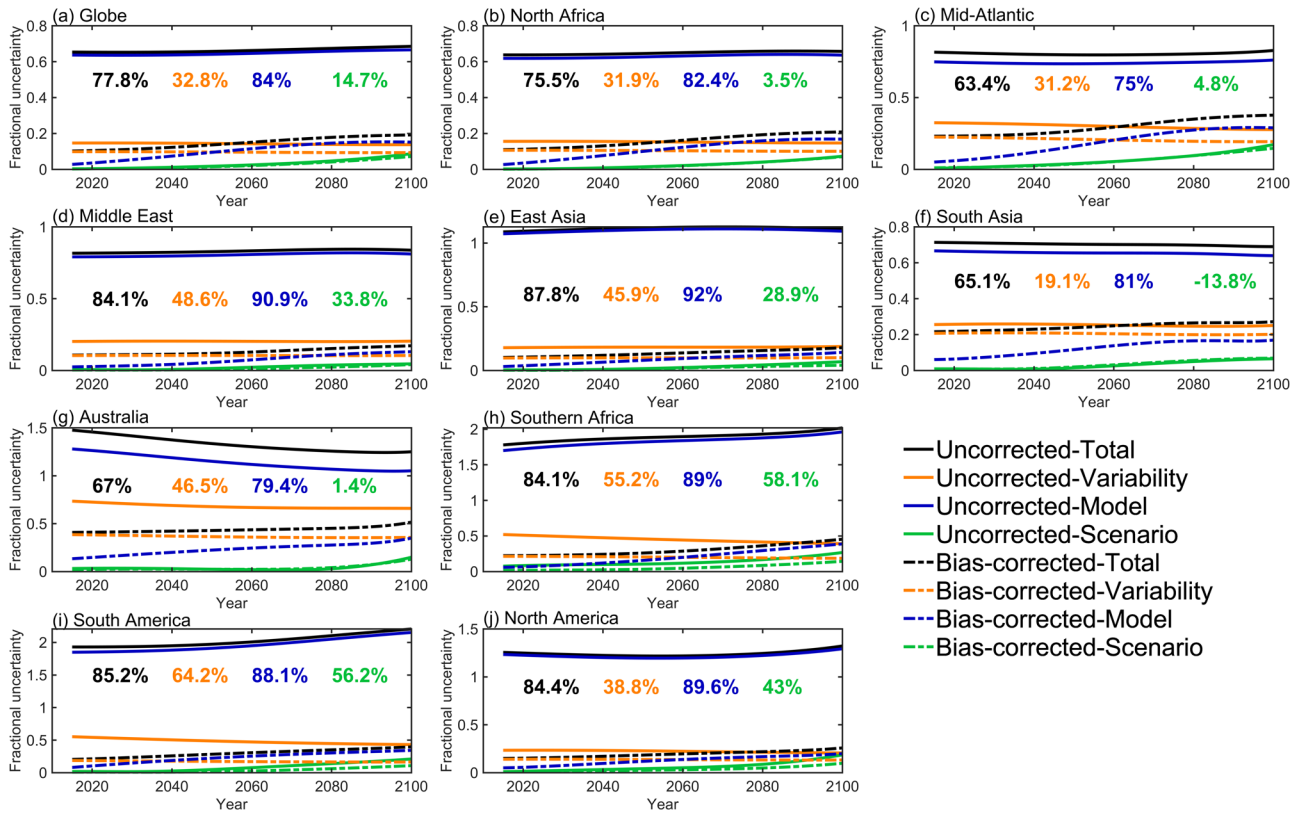


**Fig. 7 The evolution of uncertainty components.** The fractional uncertainty of each component in decadal mean projections (the 90% confidence level divided by the mean projection) for DML over the globe (a) and nine study regions (b–j). Black, orange, blue, and green denote total uncertainty, internal variability, model uncertainty, and scenario uncertainty, respectively. The solid and dotted lines are uncorrected and bias-corrected results, respectively. The numbers within each panel are relative reductions in uncertainty after bias correction compared to before bias correction.

mass density, AOD, and dust AOD) from 1980 to 2021<sup>90</sup>. This product is available on a  $0.5^\circ \times 0.625^\circ$  grid, and is freely available at [https://gmao.gsfc.nasa.gov/reanalysis/MERRA-2/data\\_access/](https://gmao.gsfc.nasa.gov/reanalysis/MERRA-2/data_access/).

### CMIP6 climate models

Compared with previous CMIP projects, the CMIP6 project contains the greatest number of climate models, the most extensive numerical experiments, and the most extensive simulation data, with 112 climate models originating from 33 institutions worldwide. In this study, limited by data availability, 10 CMIP6 models were used to capture the seasonal to decadal variations in global DML, including historical simulations for 1980–2014 and the SSP126, SSP245, SSP370, and SSP585 scenarios for 2015–2100. In addition, we used monthly data on dust emissions, dust wet deposition, precipitation, soil moisture content, and surface wind speed for five models (GISS-E2-1-G, GISS-E2-1-H, MIROC-ES2L, MIROC6, and MRI-ESM2-0). Note that the output of all models and MERRA2 reanalysis data were interpolated onto a common  $1^\circ \times 1^\circ$  grid to unify the resolution. Supplementary Table 1 provides a summary of the models used in this study; further information can be found at <https://esgf-node.llnl.gov/search/cmip6/>.

### MODIS satellite data

The Moderate Resolution Imaging Spectroradiometer (MODIS) carries the NASA's twin polar satellites of Terra and Aqua, which provide near-global high-quality aerosol data almost on a daily since 2000 and 2002 respectively<sup>91</sup>. We use monthly MODIS-Terra Level 3 retrievals over the period 2003–2021 with a resolution of  $1^\circ \times 1^\circ$ , and

it is available for free at <https://ladsweb.modaps.eosdis.nasa.gov/search/order/>.

The Collection 5.1 MODIS global land cover type product (MCD12C1) provides global distribution of land cover types with a resolution of  $0.05^\circ \times 0.05^\circ$ . It is obtained by supervised classification of reflectivity from MODIS's Terra and Aqua satellites, and then further optimized for specific categories with post-processing and auxiliary information. The dataset includes 17 surface vegetation types developed by the International Geosphere–Biosphere Programme (IGBP)<sup>92</sup>. It is used in this study to identify dust source regions, and is available at <https://modis.gsfc.nasa.gov/data/dataproduct/mod12.php>.

### Calculation of MODIS dust mass loading

To verify the effect of model bias correction, we calculated the MODIS dust optical depth (DOD) for 2003–2021 by combining MERRA2 and MODIS aerosol products using the method developed by Gkikas et al.<sup>93</sup>. The method mainly considered that the MERRA2 dust fraction (MDF) to total  $AOD_{550nm}$  is also applicable to MODIS products, and the specific calculation formula is as follows:

$$MDF = \frac{AOD_{dust;MERRA2}}{AOD_{total;MERRA2}} \quad (1)$$

$$DOD_{MODIS} = AOD_{MODIS} \times MDF \quad (2)$$

where climatological *MDF* is calculated spatially during the period of 2003–2021 at a  $1^\circ \times 1^\circ$  spatial resolution. Gkikas et al.<sup>93</sup> indicated that the MODIS DOD data is well correlated with



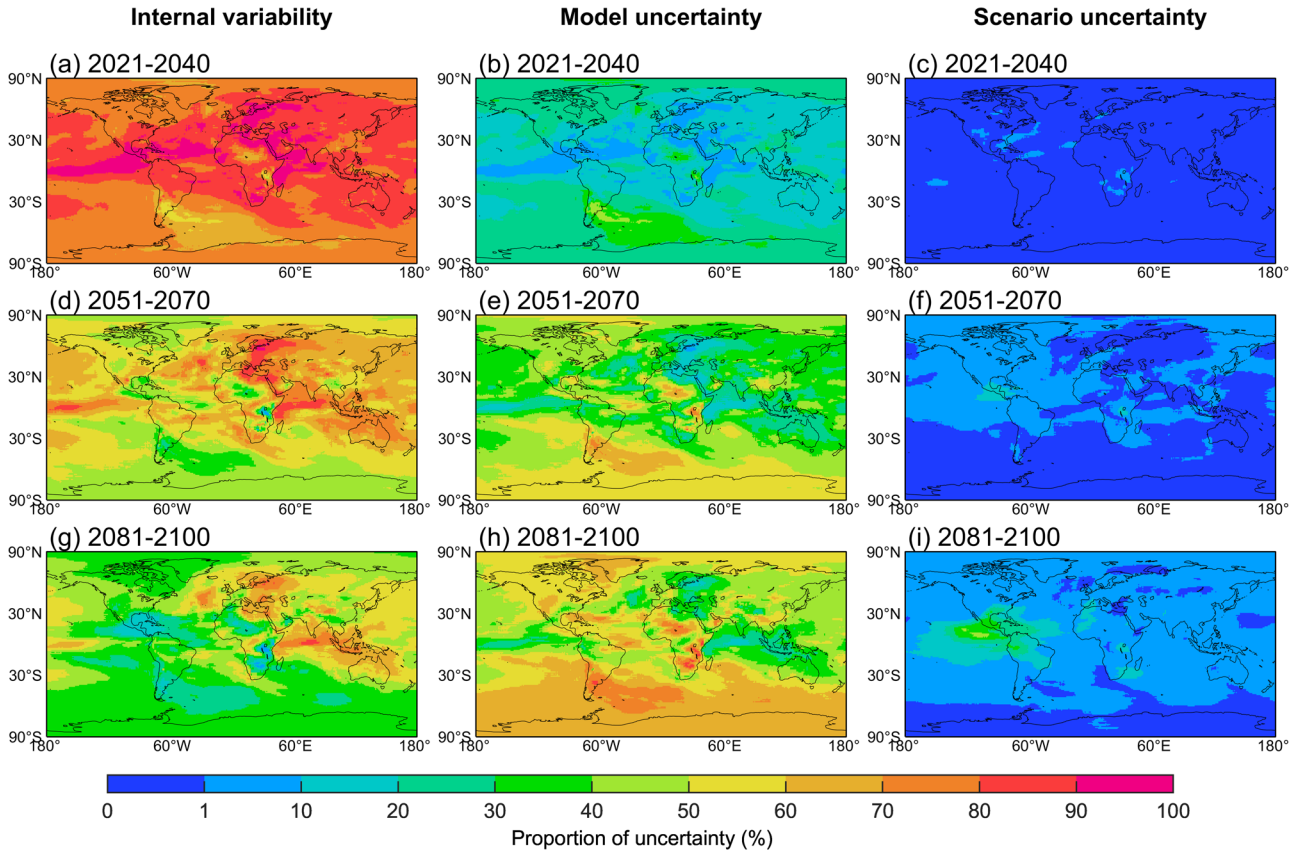


**Fig. 8** Spatial distribution for proportion of uncertainty. Proportion of uncertainty of three uncertainty sources (internal variability, model uncertainty and scenario uncertainty) in projections of multidecadal mean DML based on bias-corrected CMIP6 models. The columns show the total variance explained by (left) internal variability, (middle) model uncertainty, and (right) scenario uncertainty for predictions of the (a–c) near-term (2021–2040), (d–f) medium-term (2051–2070), and (g–i) long-term (2081–2100).

AERONET-derived DOD with a correlation coefficient of 0.89, and a small bias of 0.004 (2.7 %).

The conversion from DOD ( $\tau$ ) to DML (M) is calculated as follows<sup>94</sup>:

$$M = \frac{4 \rho r_{\text{eff}}}{3 Q_{\text{ext}}} \tau = \frac{1}{\epsilon} \tau \quad (3)$$

where  $\rho$  is the density of dust,  $r_{\text{eff}}$  is the dust effective radius,  $Q_{\text{ext}}$  is the dust extinction efficiency, and  $\epsilon$  is the mass extinction efficiency. We used the empirical values suggested by Ginoux et al.<sup>78</sup> and assumed  $\rho = 2600 \text{ kg} \cdot \text{m}^{-3}$ ,  $r_{\text{eff}} = 1.2 \mu\text{m}$ ,  $Q_{\text{ext}} = 2.5$ ,  $\epsilon = 0.6 \text{ m}^2\text{g}^{-1}$ , and  $\tau$  is the MODIS DOD.

### EDCDF bias-corrected method

As reported by Li et al.,<sup>71</sup> the EDCDF method requires establishing a cumulative distribution function (CDF) for the observations, historical simulation, and future projection. The EDCDF method used in this study improves on previous historical CDF-based method and applies quantile-based CDF mapping between historical and projected periods<sup>57,58,95</sup>. Based on the large differences in DML spatial distribution, the bias correction is applied as follows.

$$x_{m-p_{\text{adjust}}} = x_{m-p} + F_{o-t}^{-1}[F_{m-p}(x_{m-p})] - F_{m-t}^{-1}[F_{m-p}(x_{m-p})] \quad (4)$$

where  $x_{m-p_{\text{adjust}}}$  is the projected value of the adjusted model after bias correction;  $x_{m-p}$  is the projected value of initial model;  $F_{m-p}$  is the CDF of the model simulated fields;  $F_{o-t}^{-1}$  and  $F_{m-t}^{-1}$  are the quantile functions corresponding to the MERRA2 reanalysis  $o$  and CMIP6 simulation  $m$  in the training period  $t$ , respectively.

The two-parameter gamma distribution is used for the part of a given time series  $x$  with dust aerosol:

$$f(x; k, \theta) = x^{k-1} \frac{e^{-x/\theta}}{\theta^k \Gamma(k)} \text{ for } x > 0 \text{ and } k, \theta > 0 \quad (5)$$

where  $k$  is a shape parameter,  $\theta$  is a scale parameter, and  $\Gamma(k)$  is the Gamma function.

The purpose of this study is to demonstrate the application of the EDCDF method to 10 CMIP6 models for global DML in the historical simulations and future projections. Here parametric distributions were fitted to DML fields at each grid point. Given that MERRA2 assimilated MODIS satellite observation from 2000 onwards, the CMIP6 models were calibrated for the training period (2000–2014). For future projections, we examined the short-term (2021–2040), medium-term (2051–2070), and long-term (2081–2100) changes compared with the historical period (2000–2014) under the four SSP scenarios. For further details of this method, see Li et al.<sup>71</sup> and Yang et al.<sup>57,58</sup>.

### Taylor skill score method

We use the Taylor diagram method<sup>75</sup> to evaluate the performance of the initial and bias-corrected CMIP6 space fields relative to the MERRA2 reanalysis climatology. The Taylor diagram is a common method for systematically comparing correlation coefficient (CC), standard deviation (SD), and root-mean-square error (RMSE) values, which can effectively reflect the advantages and disadvantages of each model simulation. In Taylor diagram, a smaller distance between the models and the MERRA2 indicates a better

agreement. In addition, we apply the skill score (SS) to quantify the performance of each model in the historical period. Here the SS is defined as follows:

$$SS = \frac{4(1 + CC)^4}{(NSD_m + \frac{1}{NSD_m})^2(1 + CC_0)^4} \quad (6)$$

where the normalized SD (NSD) is defined as the ratio of the standard deviation of model simulated and MERRA2 reanalyzed climatology;  $m$  stands for model simulation;  $NSD_m$  is the normalized standard deviation of the simulation;  $CC$  is the correlation coefficient between simulation and reanalysis data, and  $CC_0$  is the maximum correlation coefficient. The closer the SS is to 1, the stronger the ability of individual model to represent the reanalyzed result.

### Separating uncertainty sources

We used the method developed by Hawkins and Sutton<sup>76,77</sup> to partition uncertainty in DML projections, which are the internal variability, model uncertainty, and scenario uncertainty, and the detailed calculation procedures see Supplementary Text 1 in Supporting Information. Note that this identification method requires that all models under historical simulation and future projections should have the same ensemble members, thence we choose just one ensemble member for each CMIP6 model. In this study, we use 10 CMIP6 models and four future emissions scenarios to isolate the uncertainty sources.

### DATA AVAILABILITY

The MERRA2 reanalysis data is available at [https://gmao.gsfc.nasa.gov/reanalysis/MERRA-2/data\\_access/](https://gmao.gsfc.nasa.gov/reanalysis/MERRA-2/data_access/). CMIP6 outputs are available from <https://esgf-node.lnl.gov/search/cmip6/>. The MODIS-Terra Level 3 AOD is available at <https://ladsweb.modaps.eosdis.nasa.gov/search/order/>, and MODIS global land cover type product is downloaded at <https://modis.gsfc.nasa.gov/data/dataproduct/mod12.php>.

### CODE AVAILABILITY

Analysis was performed using the Matrix Laboratory (MATLAB; <https://www.mathworks.com/>), and all codes to generate the figures are available from the corresponding author.

Received: 7 July 2023; Accepted: 11 December 2023;

Published online: 02 January 2024

### REFERENCES

- Ramanathan, V., Crutzen, P. J., Kiehl, J. T. & Rosenfeld, D. Aerosols, climate, and the hydrological cycle. *Science* **294**, 2119–2124 (2002).
- Pey, J., Querol, X., Alastuey, A., Forastiere, F. & Stafoggia, M. African dust outbreaks over the Mediterranean Basin during 2001–2011: PM10 concentrations, phenomenology and trends, and its relation with synoptic and mesoscale meteorology. *Atmos. Chem. Phys.* **13**, 1395–1410 (2013).
- Che, H. et al. Column aerosol optical properties and aerosol radiative forcing during a serious haze-fog month over East Asia Plain in 2013 based on ground-based sunphotometer measurements. *Atmos. Chem. Phys.* **14**, 2125–2138 (2014).
- Che, H. et al. Analyses of aerosol optical properties and direct radiative forcing over urban and industrial regions in northeast China. *Meteorol. Atmos. Phys.* **127**, 345–354 (2015).
- Huang, J., Liu, J., Chen, B. & Nasiri, S. L. Detection of anthropogenic dust using CALIPSO lidar measurements. *Atmos. Chem. Phys.* **15**, 11653–11665 (2015).
- Rodríguez, S., Riera, R., Fonteneau, A., Alonso-Pérez, S. & López-Darías, J. African desert dust influences migrations and fisheries of the Atlantic skipjack-tuna. *Atmos. Environ.* **312**, 120022 (2023).
- Martínez-García, A. et al. Links between iron supply, marine productivity, sea surface temperature, and CO<sub>2</sub> over the last 1.1 Ma. *Paleoceanography* **24**, PA1207 (2009).
- Tanaka, T. Y. & Chiba, M. A numerical study of the contributions of dust source regions to the global dust budget. *Glob. Planet. Change* **52**, 88–104 (2006).
- Froyd, K. D. et al. Dominant role of mineral dust in cirrus cloud formation revealed by global-scale measurements. *Nat. Geosci.* **15**, 1–7 (2022).
- Zender, C. S., Miller, R. L. & Tegen, I. Quantifying mineral dust mass budgets: terminology, constraints, and current estimates. *EOS Trans. Am. Geophys. Union* **85**, 509–512 (2004).
- Shao, Y. et al. Dust cycle: An emerging core theme in Earth system science. *Aeolian Res.* **2**, 181–204 (2011).
- Charlson, R. J. & Heizenberg, J. *Aerosol Forcing of Climate* (John Wiley & Sons Press, 1995).
- Houghton, J. T. et al. *Climate Change 2001: The Scientific Basis* (Cambridge University Press, 2001).
- IPCC, 2013: Climate Change 2013. *The Physical Science Basis. Contribution of Working Group I to the Fifth Assessment Report of the Intergovernmental Panel on Climate Change* (Cambridge University Press, 2013).
- Uno, I. et al. Asian dust transported one full circuit around the globe. *Nat. Geosci.* **2**, 557–56 (2009).
- Francis, D. et al. Atmospheric rivers drive exceptional Saharan dust transport towards Europe. *Atmos. Res.* **266**, 105959 (2022).
- Gandham, H., Dasari, H. P., Karumuri, A., Ravuri, P. M. K. & Hoteit, I. Three-dimensional structure and transport pathways of dust aerosols over West Asia. *npj Clim. Atmos. Sci.* **5**, 45 (2022).
- Gkikas, A. et al. Quantification of the dust optical depth across spatiotemporal scales with the MIDAS global dataset (2003–2017). *Atmos. Chem. Phys.* **22**, 3553–3578 (2022).
- Han, Y. et al. New insights into the Asian dust cycle derived from CALIPSO lidar measurements. *Remote Sens. Environ.* **272**, 112906 (2022).
- Zhao, X., Huang, K., Fu, J. S. & Abdullaev, S. F. Long-range transport of Asian dust to the Arctic: identification of transport pathways, evolution of aerosol optical properties, and impact assessment on surface albedo changes. *Atmos. Chem. Phys.* **22**, 10389–10407 (2022).
- García, M. I., Rodríguez, S. & Alastuey, A. Impact of North America on the aerosol composition in the North Atlantic free troposphere. *Atmos. Chem. Phys.* **17**, 7387–7404 (2017).
- Prospero, J. M., Ginoux, P., Torres, O., Nicholson, S. E. & Gill, T. E. Environmental characterization of global sources of atmospheric soil dust identified with the nimbus 7 total ozone mapping spectrometer (TOMS) absorbing aerosol product. *Rev. Geophys.* **40**, 1–30 (2002).
- Huebert, B. J. et al. An overview of ACE-Asia: Strategies for quantifying the relationships between Asian aerosols and their climatic impacts. *J. Geophys. Res. Atmos.* **108**, 8633 (2003).
- Wang, X., Huang, J., Zhang, R., Chen, B. & Bi, J. Surface measurements of aerosol properties over northwest China during ARM China 2008 deployment. *J. Geophys. Res. Atmos.* **115**, D00K27 (2010).
- Che, H. et al. Ground-based aerosol climatology of China: Aerosol optical depths from the China Aerosol Remote Sensing Network (CARSNET) 2002–2013. *Atmos. Chem. Phys.* **15**, 7619–7652 (2015).
- Wang, X. et al. A comparison of the physical and optical properties of anthropogenic air pollutants and mineral dust over northwest China. *J. Meteorol. Res.* **29**, 180–200 (2015).
- Chen, Q. et al. Enhanced health risks from exposure to environmentally persistent free radicals and the oxidative stress of PM2.5 from Asian dust storms in Erenhot, Zhangbei and Jinan, China. *Environ. Int.* **121**, 260–268 (2018).
- Wang, X., Liu, J., Che, H., Ji, F. & Liu, J. Spatial and temporal evolution of natural and anthropogenic dust events over northern China. *Sci. Rep.* **8**, 2141 (2018).
- Wang, X. et al. Optical and microphysical properties of natural mineral dust and anthropogenic soil dust near dust source regions over northwestern China. *Atmos. Chem. Phys.* **18**, 2119–2138 (2018).
- Che, H. et al. Spatial distribution of aerosol microphysical and optical properties and direct radiative effect from the China Aerosol Remote Sensing Network. *Atmos. Chem. Phys.* **19**, 11843–11864 (2019).
- Kaufman, Y. J., Tanré, D. & Boucher, O. A satellite view of aerosols in the climate system. *Nature* **419**, 215–223 (2002).
- Han, H. J. & Sohn, B. J. Retrieving Asian dust AOT and height from hyperspectral sounder measurements: an artificial neural network approach. *J. Geophys. Res. Atmos.* **118**, 837–845 (2013).
- Jin, Q., Wei, J. & Yang, Z. L. Positive response of Indian summer rainfall to middle East dust. *Geophys. Res. Lett.* **41**, 4068–4074 (2014).
- Jin, Q., Wei, J., Yang, Z. L., Pu, B. & Huang, J. Consistent response of Indian summer monsoon to Middle East dust in observations and simulations. *Atmos. Chem. Phys.* **15**, 9897–9915 (2015).
- Liu, J., Wu, D., Wang, T., Ji, M. & Wang, X. Interannual variability of dust height and the dynamics of its formation over East Asia. *Sci. Total Environ.* **751**, 142288 (2020).

36. Mukai, M., Nakajima, T. & Takemura, T. A study of long-term trends in mineral dust aerosol distributions in Asia using a general circulation model. *J. Geophys. Res. Atmos.* **109**, D19204 (2004).
37. Mao, R., Ho, C. H., Shao, Y., Gong, D. Y. & Kim, J. Influence of Arctic Oscillation on dust activity over northeast Asia. *Atmos. Environ.* **45**, 326–337 (2011).
38. Wu, C., Lin, Z., Shao, Y., Liu, X. & Li, Y. Drivers of recent decline in dust activity over East Asia. *Nat. Commun.* **13**, 7105 (2022).
39. Ginoux, P., Prospero, J. M., Torres, O. & Chin, M. Long-term simulation of global dust distribution with the GOCART model: correlation with North Atlantic Oscillation. *Environ. Modell. Softw.* **19**, 113–128 (2004).
40. Pu, B. & Ginoux, P. How reliable are CMIP5 models in simulating dust optical depth? *Atmos. Chem. Phys.* **18**, 12491–12510 (2018).
41. Wang, Z. et al. Incorrect Asian aerosols affecting the attribution and projection of regional climate change in CMIP6 models. *npj Clim. Atmos. Sci.* **4**, 2 (2021).
42. Wu, C. et al. Can climate models reproduce the decadal change of dust aerosol in East Asia? *Geophys. Res. Lett.* **45**, 9953–9962 (2018).
43. Wu, C., Lin, Z. & Liu, X. The global dust cycle and uncertainty in CMIP5 (Coupled Model Intercomparison Project phase 5) models. *Atmos. Chem. Phys.* **20**, 10401–10425 (2020).
44. Aryal, Y. N. & Evans, S. Global dust variability explained by drought sensitivity in CMIP6 models. *J. Geophys. Res.-Earth* **126**, e2021JF006073 (2021).
45. Zhao, Y. et al. Multi-model ensemble projection of the global dust cycle by the end of 21st century using the Coupled Model Intercomparison Project version 6 data. *Atmos. Chem. Phys.* **23**, 7823–7838 (2023).
46. Kok, J. F. et al. Mineral dust aerosol impacts on global climate and climate change. *Nat. Rev. Earth Environ.* **4**, 71–86 (2023).
47. Zhao, A., Ryder, C. L. & Wilcox, L. J. How well do the CMIP6 models simulate dust aerosols? *Atmos. Chem. Phys.* **22**, 2095–2119 (2022).
48. Weigel, A. P., Knutti, R., Liniger, M. & Appenzeller, C. Risks of model weighting in multimodel climate projections. *J. Clim.* **23**, 4175–4191 (2010).
49. Knutti, R. et al. A climate model projection weighting scheme accounting for performance and interdependence. *Geophys. Res. Lett.* **44**, 1909–1918 (2017).
50. IPCC, 2021: *Climate Change 2021. The Physical Science Basis. Contribution of Working Group I to the Sixth Assessment Report of the Intergovernmental Panel on Climate Change* (Cambridge University Press, 2021).
51. Brunner, L. et al. Reduced global warming from CMIP6 projections when weighting models by performance and independence. *Earth Syst. Dyn.* **11**, 995–1012 (2020).
52. Stott, P., Good, P., Jones, G., Gillett, N. & Hawkins, E. The upper end of climate model temperature projections is inconsistent with past warming. *Environ. Res. Lett.* **8**, 014024 (2013).
53. Gillett, N. P. et al. Constraining human contributions to observed warming since the pre-industrial period. *Nat. Clim. Change* **11**, 207–212 (2021).
54. Hall, A., Cox, P., Huntingford, C. & Klein, S. Progressing emergent constraints on future climate change. *Nat. Clim. Change* **9**, 269–278 (2019).
55. Briant, F. Reducing uncertainties in climate projections with emergent constraints: concepts, examples and prospects. *Adv. Atmos. Sci.* **37**, 1–15 (2020).
56. Chen, Z. et al. Observationally constrained projection of Afro-Asian monsoon precipitation. *Nat. Commun.* **13**, 2552 (2022).
57. Yang, X. et al. Bias correction of historical and future simulations of precipitation and temperature for China from CMIP5 models. *J. Hydrometeorol.* **19**, 609–623 (2018).
58. Yang, X. et al. The optimal multimodel ensemble of bias-corrected CMIP5 climate models over China. *J. Hydrometeorol.* **21**, 845–863 (2020).
59. Mishra, V., Bhatia, U. & Tiwari, A. D. Bias-corrected climate projections for South Asia from Coupled Model Intercomparison Project-6. *Sci. Data* **7**, 338 (2020).
60. Sun, Y. et al. Rapid increase in the risk of extreme summer heat in eastern China. *Nat. Clim. Change* **4**, 1082–1085 (2014).
61. Siler, N., Po-Chedley, S. & Bretherton, C. S. Variability in modeled cloud feedback tied to differences in the climatological spatial pattern of clouds. *Clim. Dyn.* **50**, 1209–1220 (2018).
62. Brunner, L. et al. Comparing methods to constrain future European climate projections using a consistent framework. *J. Clim.* **33**, 8671–8692 (2020).
63. Tokarska, K. B. et al. Past warming trend constrains future warming in CMIP6 models. *Sci. Adv.* **6**, eaaz9549 (2020).
64. Freychet, N., Hegerl, G., Mitchell, D. & Collins, M. Future changes in the frequency of temperature extremes may be underestimated in tropical and subtropical regions. *Commun. Earth Environ.* **2**, 28 (2021).
65. Zhou, T. New physical science behind climate change: What does IPCC AR6 tell us? *Innovation* **2**, 100173 (2021).
66. Lee, J. Y. et al. Future global climate: Scenariobased projections and near-term information//IPCC. *Climate Change 2021: The Physical Science Basis. Contribution of Working Group I to the Sixth Assessment Report of the Intergovernmental Panel on Climate Change* (Cambridge University Press, 2021).
67. Navarro-Racines, C., Tarapues, J., Thornton, P., Jarvis, A. & Ramirez-Villegas, J. High-resolution and bias-corrected CMIP5 projections for climate change impact assessments. *Sci. Data* **7**, 7 (2020).
68. Hu, S. & Zhou, T. Skillful prediction of summer rainfall in the Tibetan Plateau on multi-year timescales. *Sci. Adv.* **7**, eabf9395 (2021).
69. Panofsky, H. A. & Brier, G. W. *Some Application of Statistics to Meteorology* (Pennsylvania State University, 1958).
70. Gudmundsson, L., Bremnes, J. B., Haugen, J. E. & Skaugen, T. E. Technical Note: Downscaling RCM precipitation to the station scale using statistical transformations—a comparison of methods. *Hydrol. Earth Syst. Sci.* **16**, 3383–3390 (2012).
71. Li, H., Sheffield, J. & Wood, E. F. Bias correction of monthly precipitation and temperature fields from Intergovernmental Panel on Climate Change AR4 models using equidistant quantile matching. *J. Geophys. Res. Atmos.* **115**, D10101 (2010).
72. Liu, J. et al. Impact of Arctic amplification on declining spring dust events in East Asia. *Clim. Dyn.* **54**, 1913–1935 (2019).
73. Buchard, V. et al. The MERRA-2 aerosol reanalysis, 1980-onward, part II: evaluation and case studies. *J. Clim.* **30**, 6851–6872 (2017).
74. Randles, C. A. et al. The MERRA-2 aerosol reanalysis, 1980-onward, part I: system description and data assimilation evaluation. *J. Clim.* **30**, 6823–6850 (2017).
75. Taylor, K. E. Summarizing multiple aspects of model performance in a single diagram. *J. Geophys. Res. Atmos.* **106**, 7183–7192 (2001).
76. Hawkins, E. & Sutton, R. The potential to narrow uncertainty in regional climate predictions. *Bull. Am. Meteorol. Soc.* **90**, 1095–1108 (2009).
77. Hawkins, E. & Sutton, R. The potential to narrow uncertainty in projections of regional precipitation change. *Clim. Dyn.* **37**, 407–418 (2011).
78. Ginoux, P., Prospero, J. M., Gill, T. E., Hsu, N. C. & Zhao, M. Global-scale attribution of anthropogenic and natural dust sources and their emission rates based on MODIS deep blue aerosol products. *Rev. Geophys.* **50**, RG3005 (2012).
79. Kok, J. et al. Contribution of the world's main dust source regions to the global cycle of desert dust. *Atmos. Chem. Phys.* **21**, 8169–8193 (2021).
80. Ridley, D. A., Heald, C. L. & Prospero, J. M. What controls the recent changes in African mineral dust aerosol across the Atlantic? *Atmos. Chem. Phys.* **14**, 5735–5747 (2014).
81. Xia, W., Wang, Y. & Wang, B. Decreasing dust over the Middle East partly caused by irrigation expansion. *Earths Future* **10**, e2021EF002252 (2022).
82. Li, J. et al. Predominant type of dust storms that influences air quality over northern China and future projections. *Earth's Future* **10**, e2022EF002649 (2022).
83. Mytilinaios, M. et al. Comparison of dust optical depth from multi-sensor products and MONARCH (Multiscale Online Non-hydrostatic Atmosphere Chemistry) dust reanalysis over North Africa, the Middle East, and Europe. *Atmos. Chem. Phys.* **23**, 5487–5516 (2023).
84. Evan, A. T. Surface winds and dust biases in climate models. *Geophys. Res. Lett.* **45**, 1079–1085 (2018).
85. Evan, A. T., Flamant, C., Gaetani, M. & Guichard, F. The past, present and future of African dust. *Nature* **531**, 493–495 (2016).
86. Yuan, T. L. et al. Positive low cloud and dust feedbacks amplify tropical North Atlantic Multidecadal Oscillation. *Geophys. Res. Lett.* **43**, 1349–1356 (2016).
87. Doherty, O. M., Riemer, N. & Hameed, S. Saharan mineral dust transport into the Caribbean: observed atmospheric controls and trends. *J. Geophys. Res.* **113**, 1–10 (2008).
88. DeFlorio, M. J. et al. Interannual modulation of subtropical Atlantic boreal summer dust variability by ENSO. *Clim. Dyn.* **46**, 1–15 (2015).
89. Colarco, P., da Silva, A. M., Chin, M. & Diehl, T. Online simulations of global aerosol distributions in the NASA GEOS-4 model and comparisons to satellite and ground-based aerosol optical depth. *J. Geophys. Res. Atmos.* **115**, D14207 (2010).
90. Global Modeling and Assimilation Office (GMAO) MERRA-2 avgM\_2d\_aer\_Nx: 2d, Monthly mean, Time-averaged, Single-Level, Assimilation, Aerosol Diagnostics V5.12.4, Greenbelt, MD, USA: Goddard Space Flight Center Distributed Active Archive Center (GSFC DAAC), Accessed on 28 September 2022. <https://doi.org/10.5067/FH9A0MLJPC7N> (2015).
91. Levy, R. C. et al. The Collection 6 MODIS aerosol products over land and ocean. *Atmos. Meas. Tech.* **6**, 2989–3034 (2013).
92. Friedl, M. A. et al. MODIS Collection 5 global land cover: algorithm refinements and characterization of new datasets. *Remote Sens. Environ.* **114**, 168–182 (2010).
93. Gkikas, A. et al. ModIs Dust AeroSol (MIDAS): a global fine-resolution dust optical depth data set. *Atmos. Meas. Tech.* **14**, 309–334 (2021).
94. Ginoux, P. et al. Sources and distributions of dust aerosols simulated with the GOCART model. *J. Geophys. Res.* **106**, 20255–20273 (2001).
95. Aloysius, N. R., Sheffield, J., Sifers, J. E., Li, H. & Wood, E. F. Evaluation of historical and future simulations of precipitation and temperature in central Africa from CMIP5 climate models. *J. Geophys. Res. Atmos.* **121**, 130–152 (2016).

## ACKNOWLEDGEMENTS

This work is supported by the National Natural Science Foundation of China (42205081, and 41875091), and the China Postdoctoral Science Foundation (2021M701522).

## AUTHOR CONTRIBUTIONS

J.L.: conceptualization, methodology, writing original draft, and funding acquisition; X.W.: methodology and data analysis; D.W., and H.W.: data curation and formal analysis; Y.L.: conceptualization and writing; M.J.: conceptualization and funding acquisition. All authors contributed to the review and improvement of the manuscript.

## COMPETING INTERESTS

The authors declare no competing interests.

## ADDITIONAL INFORMATION

**Supplementary information** The online version contains supplementary material available at <https://doi.org/10.1038/s41612-023-00550-9>.

**Correspondence** and requests for materials should be addressed to Yu Li or Mingxia Ji.

**Reprints and permission information** is available at <http://www.nature.com/reprints>

**Publisher's note** Springer Nature remains neutral with regard to jurisdictional claims in published maps and institutional affiliations.



**Open Access** This article is licensed under a Creative Commons Attribution 4.0 International License, which permits use, sharing, adaptation, distribution and reproduction in any medium or format, as long as you give appropriate credit to the original author(s) and the source, provide a link to the Creative Commons license, and indicate if changes were made. The images or other third party material in this article are included in the article's Creative Commons license, unless indicated otherwise in a credit line to the material. If material is not included in the article's Creative Commons license and your intended use is not permitted by statutory regulation or exceeds the permitted use, you will need to obtain permission directly from the copyright holder. To view a copy of this license, visit <http://creativecommons.org/licenses/by/4.0/>.

© The Author(s) 2024